Draft version February 2, 2008
Preprint typeset using LaTeX style emulateapj v. 11/12/01

DETECTING INTRACLUSTER GAS MOTION IN GALAXY CLUSTERS: MOCK *ASTRO-E2* OBSERVATIONS

Andrew Pawl[1], August E. Evrard[1,2,3], Renato A. Dupke[1,2]
apawl@umich.edu, evrard@umich.edu, rdupke@umich.edu
Draft version February 2, 2008

ABSTRACT

We explore the detectability of bulk motions in the X-ray emitting intracluster medium (ICM) using a catalog of 1,836 mock *Astro-E2* observations of simulated clusters of galaxies. We generate high resolution mock spectra for two observing strategies: a four-pointing mosaic and a single central pointing. Normalizing to 200 (400) photons in the iron Kα region for the mosaic (central) study, we fit Poisson realizations of each simulated spectrum to a velocity broadened isothermal plasma emission model. We confirm that the velocity characteristics (mean and dispersion) returned by the spectral fittings are unbiased measures of the emission-weighted values within the observed region, with scatter ± 55 km s^{-1}. The maximum velocity difference between mosaic element pairs $\Delta v_{\rm max}$ has $\sim 6\%$ likelihood of being transonic ($\Delta v_{\rm max} \geq 0.5 c_s$), and the likelihood falls steeply, $p \propto (\Delta v_{\rm max}/c_s)^{-4}$, at high Mach number. The velocity broadening parameter σ_v from the central pointing fit exceeds the thermal value in 49% of the cases, with again a σ_v^{-4} tail at large dispersion. We present as case studies the clusters that yield the strongest signal for each observing strategy.

Subject headings: clusters: general — clusters: ICM — cosmology: observations — intergalactic medium — X-rays: clusters

1. INTRODUCTION

In a hierarchical model of structure formation, galaxy clusters are built from the continuous accretion of subsystems and, therefore, clusters are expected to frequently display visible signatures of mergers. Binary clusters (Jones & Forman 1984) offer evidence of precursor systems while clusters with multiple emissivity peaks, strong isophotal twists and ellipticity variations possess morphologies associated with the later stages of merger evolution (Mohr, Fabricant & Geller 1993; Buote & Tsai 1996). Bulk motions and turbulence of the hot intracluster medium (ICM) are thus expected to be evident in line emission from the plasma, in particular from helium-like iron, FeXXV (Dupke & Bregman 2001a,b; Sunyaev et al. 2003; Inogamov & Sunyaev 2003).

X-ray satellite missions to date have had spectrometers with energy resolutions marginally adequate for the observation of cluster velocity structure (Dupke & Bregman 2001a,b). The new microcalorimeter technology employed in the X-ray Spectrometer (XRS) instrument aboard the *Astro-E2* satellite, however, is designed to have an energy resolution of 6.5 eV FWHM across its entire frequency range (Furusho et al. 2004), giving a response contribution to the line broadening of $\sim$1.5 eV and finding line centroids to within about 2 eV. This implies that the instrument will be sensitive to velocity structure down to $\sim$100 km/s near the Fe Kα line. Since the infall velocity of material accreting onto a large cluster can be an order of magnitude larger than this limit, *Astro-E2* will enable unambiguous observation of gas motion in dynamically active systems.

Cosmological simulations provide a framework for investigating the statistical properties of the internal gas velocity distribution. In addition, access to the complete 3-D structure and time evolution of the simulated clusters can, through comparative studies of observations and simulations, help unfold the evolutionary history and dynamical state of observed clusters.

Until now, no estimate of the frequency with which clusters should show detectable velocity structure has been made, although Fujita et al. (2005) have used mock observations of simulated clusters to evaluate the detectability of turbulence in a specific case study. In this paper, we evaluate the fraction of clusters expected to show observable structure in the Fe Kα line by performing mock *Astro-E2* observations of a catalog of simulated clusters. The simulations model clusters in a ΛCDM cosmology with a preheated assumption for the ICM that matches observed local scaling laws (Bialek, Evrard & Mohr 2001).

In §2, we describe the simulation sample and the strategies we use to produce mock observations. Results in the form of statistical expectations and illustrative examples are presented in §3. We summarize our findings in §4.

2. MOCK OBSERVATIONS

2.1. *Preheated Cluster Simulations*

We use a catalog of 68 clusters evolved with P3MSPH (Evrard 1988) under a preheated assumption for the ICM. The level of entropy introduced into the initial conditions is tuned to 105.9 keV cm^2 in order to match the observed scalings of luminosity and ICM mass with temperature (Bialek et al. 2001).

The simulations were produced using a multi-step procedure outlined in Bialek et al. (2001). The underlying cosmology is a flat, concordance model with $\Omega_m = 0.3$, $\Omega_\Lambda = 0.7$, $\Omega_b = 0.03$, $\sigma_8 = 1.0$, and $h = 0.7$, where the

[1] Michigan Center for Theoretical Physics, University of Michigan, Ann Arbor, MI
[2] Department of Astronomy, University of Michigan, Ann Arbor, MI
[3] Department of Physics, University of Michigan, Ann Arbor, MI

Hubble constant is defined as $100h$ km s^{-1} Mpc^{-1} and σ_8 is the power spectrum normalization on $8h^{-1}$ Mpc scales. Details of the full ensemble will be presented in Bialek, Evrard & Mohr (2005). One member of the ensemble contained a prominent cold front feature, generated during a merger by the separation and resultant adiabatic cooling of the core of an infalling satellite, as discussed by Bialek, Evrard & Mohr (2002).

The cosmological values assumed for the models are in line with *WMAP* allowed parameters, with the exception of the baryon fraction. The value $\Omega_b/\Omega_m = 0.1$ used in the simulations is lower than the *WMAP* value 0.17 ± 0.01 (Bennett et al. 2003). The mass fraction in intracluster gas is expected to be less than the cosmic baryon fraction due to galaxy formation and energy exchange with dark matter during mergers (Thomas & Couchman 1992). The former process removes $\sim 15-20\%$ of the baryons from the hot phase in rich clusters while the latter expels $\sim$10% of the gas from the potential (Frenk et al. 1999). Still, the model gas fractions are likely to be somewhat low compared to current observational estimates. However, in the results presented here, the baryon fraction affects only the normalization of the ICM X-ray spectrum. Our mock spectra are tuned to a fixed line normalization, which at fixed cluster mass scales $\propto (\Omega_b/\Omega_m)^2 t_{\rm exp}$, with $t_{\rm exp}$ the exposure time. A higher or lower baryon fraction can thus be absorbed by appropriate rescaling of the exposure.

The configuration of each simulation is stored at twenty output times, spaced equally in time from the initial redshift $z_i = 20.82$ to the present. We employ the final nine outputs of the 68 models in this study, corresponding to the redshifts 0.540, 0.448, 0.365, 0.290, 0.222, 0.160, 0.102, 0.049 and 0.0. This yields 612 cluster realizations which we treat, under an ergodic hypothesis, as statistically independent. The time separation of ~ 0.7 Gyr between outputs typically exceeds the crossing time at r_{200}, justifying the ergodic assumption.

We further enhance our sample by considering the line of sight (LOS) velocity structure of each realization along three perpendicular axes. Although these projections are linked by dynamics, the LOS velocity structure is genuinely independent. We thus have three projections of each of the 612 realizations, for a total of 1,836 exposures. The members of the simulated sample range in spectral temperature from 1.5 keV to about 8 keV, with cluster masses M_{200} ranging from 0.015-2.4 $\times 10^{15} M_\odot$.

The derived spectra and images, along with associated parameters describing the simulations are publicly available as part of VCE, the *Virtual Cluster Exploratory*[4].

2.2. *Creating the Mock Exposures*

We create mock *Astro-E2* spectra of these realizations following two observing programs illustrated in Figure 1. The first program involves a search for velocity gradients by measuring differences in the mean velocity of the Fe Kα lines for multiple pointings of the *Astro-E2* instrument. This strategy allows one to measure both the magnitude and a crude direction of the velocity gradient. Multiple pointings are required because the average angular resolution of the X-ray telescopes on *Astro-E2* is $\sim$1.9′ (half-power diameter[5]) and the detector configuration is roughly a square with 2.9′ on the side. Since less than 60% of the encircled energy is contained within 2′, spatially resolved spectroscopy using sub-regions of the detector will be highly contaminated with photons from neighboring regions. Therefore, to carry out this observational strategy, we create four mock spectra of each cluster projection in a 2×2 box centered on the cluster. The second program involves searching for extra-thermal broadening of the Fe Kα line using a single, central pointing.

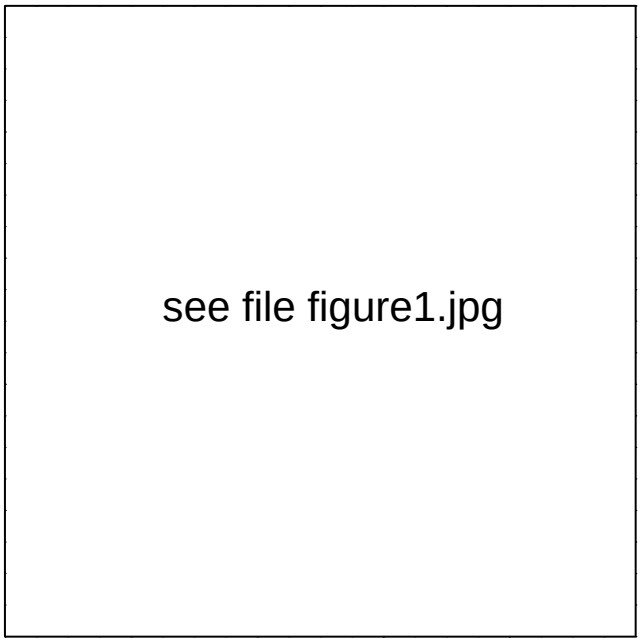

FIG. 1.— Observing strategies overlaid on the surface brightness map for a typical cluster in our catalog. The black boxes indicate the fields for the four-pointing mosaic program while the white box shows the central field of the line broadening program. Each field is 2.9 arcmin on a side, the FOV of *Astro-E2*, which corresponds to 321 kpc at $z = 0.1$.

The thermal plasma emission spectra for this study are compiled using the APEC code (Smith et al. 2001) from the XSPEC 11.3.1 suite of spectral analysis tools (Arnaud 1996). APEC allows us to include thermal broadening of the line spectra by setting the APECTHERMAL toggle to 'yes'. Further, XSPEC allows us to fold in the anticipated XRS response functions[6]. We use XSPEC/APEC to write a reference table of spectra in flux units at 176 temperatures spaced logarithmically to cover our range of interest. This spectral table is limited to an energy range appropriate for studying the Fe K complex. The final spectra are limited to the interval 5.9 keV to 6.4 keV. All spectra are generated with the cluster at a fiducial redshift of 0.1, so that the FeXXV Kα line is centered at 6.09 keV and the FeXXVI Kα line at 6.33 keV (the hydrogen-like iron line is actually two separate lines with centers at 6.32 and 6.34 keV as a result of fine structure (Verner, Verner & Ferland 1996)). Figure 2 shows the Kα line region of reference spectra at a few relevant temperatures.

To create a simulated spectrum for a mock observation, we interpolate on the reference flux table to generate

[4] http://vce.physics.lsa.umich.edu

[5] http://heasarc.gsfc.nasa.gov/docs/astroe/prop_tools/astroe2_td/

[6] obtained at http://heasarc.gsfc.nasa.gov/docs/astroe/prop_tools/xrs_mat.html

an emission spectrum for each gas particle of the simulation contained in the *Astro-E2* FOV. There are typically ~ 1000 particles in the the FOV, and their contributions are summed to obtain the complete spectrum. To convert the resulting flux spectrum into an XRS count spectrum, we first define an exposure time that requires either 200 or 400 total counts in the Fe Kα line region within the energy range of interest, i.e., 6.0-6.2 keV. (The 200 count criterion applies to the four-pointing mosaic study, while 400 counts are used for the central pointing spectra.) A single, discrete Poisson realization of each spectrum is then created, using the *poidev* routine of Press et al. (1992).

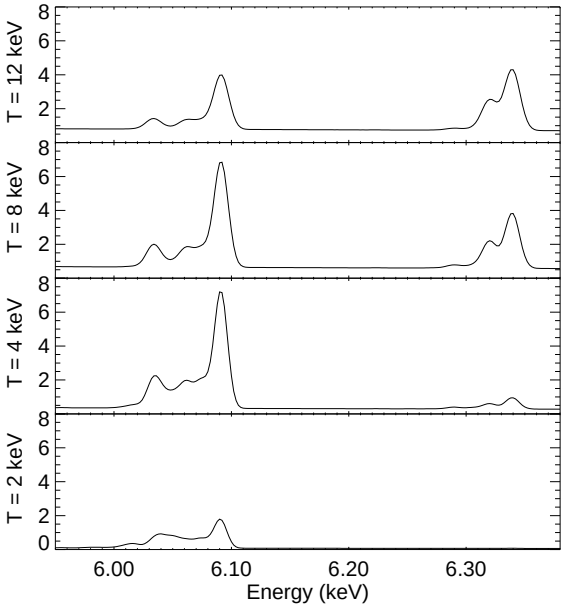

FIG. 2.— APEC thermal spectra of 0.4 solar metallicity plasma (arbitrary flux units) in a narrow energy range centered on the iron Kα complex at redshift $z = 0.1$ are shown for typical temperatures of plasma in the simulations. The *Astro-E2* XRS energy response has been folded in.

2.3. *Additional Assumptions*

The iron abundance of the ICM is not determined by cluster simulations, and so has to be assumed based on data from observed clusters. Given the small field of view of the XRS on-board *Astro-E2*, we are probing regions fairly close to the cluster's core ($\lesssim 0.2\ r_{200}$). The iron abundance in cluster cores is typically higher than the average over the whole cluster, due to the frequent presence of central metal abundance gradients in cold core ("cooling flow") clusters (Ulmer et al. 1987; White et al. 1994), which constitute the majority of clusters. Assuming an average central iron abundance of 0.27 solar for non-cold core clusters and 0.47 for cold core systems (DeGrandi et al. 2004), and recognizing that $70-90\%$ of an X-ray flux-limited sample of clusters have cold cores (Edge, Stewart & Fabian 1992), we obtain an average central iron abundance of $\sim$0.4 relative to the solar photospheric values of Anders & Grevesse (1989). This is the value assumed throughout this work.

One of the main obstacles in measuring velocities of the intracluster gas with current spectrometers is the inability to accurately calibrate the temporal and spatial fluctuations of instrumental gain, the conversion of pulse-height into photon energy (Dupke & Bregman 2001b). For the case of CCDs the intrachip (positional dependent) gain changes are related to the charge transfer inefficiency, which evolves with time. Often these fluctuations are on the same order as the velocities one is trying to measure. Although this is not an issue for the XRS calorimeter, small drifts in the temperature of the detector heat sink can cause global gain variations. The absolute precision of the gain variations in the XRS is expected to be $\sim 1-2$ eV ($50-100$ km s^{-1}) at 6 keV and will have to be inserted into the uncertainties of the velocity measurements described here (Figueroa, personal communication, 2004). These uncertainties were not incorporated in our evaluations of velocity gradients, but they do not affect the overall results derived in this work. Similarly, for the purpose of this paper we do not fake a background spectrum. The main source of background for the XRS is due to energy deposition in the detector by energetic protons. However, given the small detector size and the distribution of the proton energy spectrum, its contribution in the frequencies of interest (< 10 keV) are expected to be negligible ($<$ 2-5%) for our mock observations.

Finally, in this paper we assume that the intracluster plasma is optically thin. Gil'fanov, Sunyaev & Churazov (1987) have pointed out that this may not always be true for the Fe Kα line. Resonant scattering (the absorption and immediate re-emission of an Fe Kα line photon by an Fe ion) can be significant in the cores of clusters. If so, the line emission from the cluster core is reduced because of the scattering of photons out of the field of view. Early evidence for resonant scattering (Molendi et al. 1998) seen in the Perseus cluster has proven ambiguous, allowing other possible interpretations such as an overabundance of Ni due the central SN Ia ejecta dominance (Dupke & Arnaud 2001). *XMM* observations of the Perseus cluster have not exhibited resonant scattering in the Fe Kα line, and the absence of observed scattering has been used as evidence for the presence of turbulent (non-thermal) velocities in clusters' cores (Gastaldello & Molendi 2004, Churazov et al. 2004).

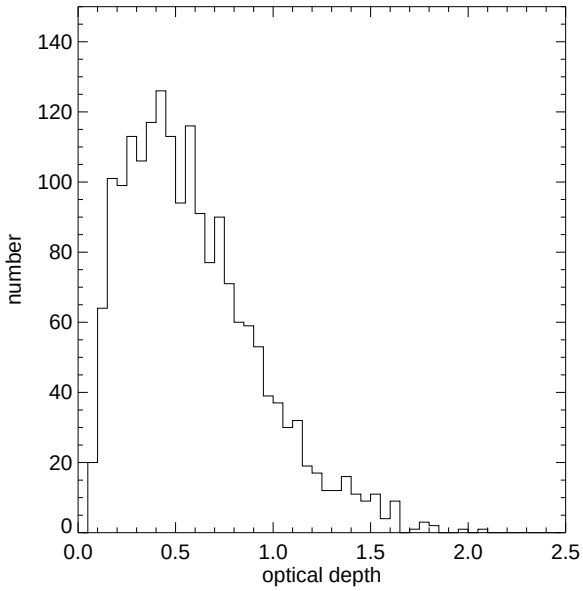

FIG. 3.— Histogram of the optical depth for the central pointing of the 1836 cluster projections used in this study.

To quantify the potential impact of resonant scattering, we compute the optical depth for the central pointing of each cluster projection used in this study (see Appendix A for details). To be conservative, we calculate the optical depth through the entire cluster. The results are shown in Figure 3. When the non-thermal velocities seen in the emission line are included, the average optical depth for the FeXXV Kα line in the FOV of the central pointing is 0.59, with standard deviation 0.34. The results of Churazov et al. (2004) and Gil'fanov et al. (1987) show that for $\tau \sim 0.6$, the flux and the linewidth near the cluster core will show approximately a 15% reduction. Additionally, it is possible that some deformation of the line profile may occur (Gil'fanov et al. 1987). None of these effects would introduce errors in the line centroids we recover. The reduction in linewidth would affect our line broadening study, but, as our results will show, a 15% reduction is not prohibitive.

2.4. *Velocity Gradients Via Multiple Pointings*

We first investigate the LOS velocity structure of the simulated clusters by creating one set of four mock exposures tiled around the most bound position of the relevant cluster, as shown by boxes 1-4 in Figure 1. The mock exposures result in four separate Poisson-noise-added spectra. We rebin these spectra to ensure at least 15 counts in each bin using the *grppha* routine from the FTOOLS package[7].

We fit the grouped spectra to find the position of the centroid velocity v_i of the Fe Kα line in image i. The spectra are fit in XSPEC to a BAPEC model. BAPEC is a thermally broadened APEC that allows for additional Gaussian velocity broadening under a parameter σ_v.

The resulting centroid positions are differenced to define velocity gradients $v_{ij} = |v_i - v_j|$ among the six distinct pairs of the four pointings. Thus, from our 1,836 independent cluster projections we generate 7,344 spectra which are used to give 11,016 velocity differences.

An advantage of working with simulated clusters is our complete knowledge of the underlying velocity structure of the gas. In an isothermal cluster, the redshift of the line center could be recovered from the density-squared weighted velocity (henceforth called the EM-weighted velocity) of the emitting gas. Our simulated clusters are not isothermal, but it happens that the Fe Kα line flux is not strongly temperature dependent within the temperature range expected for hot ICM gas. The peak flux varies by only a factor of 2 over a temperature range from 3 keV to 12 keV. For this reason, an EM-weighted velocity can be regarded as a predictor of the line center that would be recovered from a spectral analysis. Therefore, as a point of comparison we also generate the EM-weighted radial velocity of each *Astro-E2* FOV directly from the simulation.

To minimize systematic issues, we find the velocity of each FOV for a given cluster projection relative to the mean value of the four FOV's for that projection. We repeat this procedure using the BAPEC redshift values. A histogram of the differences between the velocities recovered in this way from the BAPEC spectral fits and from the EM-weighted averages is shown in Figure 4. Note that the XRS instrument is expected to find line centroids with a limiting resolution of about 2 eV near the Fe Kα complex[8], which corresponds to an expected limiting accuracy of $\sim$100 km/s near the Fe Kα line. The histogram of differences has a dispersion of 54 km s^{-1}. We conclude, therefore, that 200 counts in the line (with grouping applied) results in velocity measurement accuracies very comparable to the expected 2 eV pre-launch instrument response. This result is consistent with the findings of Fujita et al. (2005).

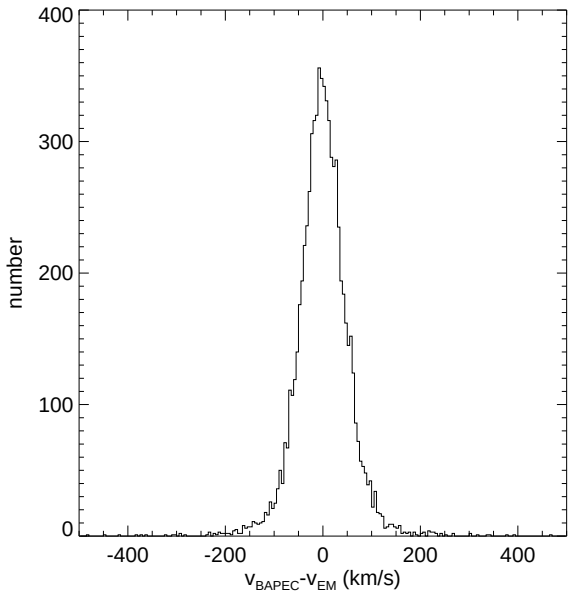

FIG. 4.— Histogram of the differences between velocities recovered from BAPEC fittings and those generated using EM-weighted velocities.

2.5. *Nonthermal Velocities Via Line Broadening*

Line broadening is another means of recovering the velocity structure of the emitting plasma. As described by Sunyaev et al. (2003) and by Inogamov & Sunyaev (2003), the large atomic mass of iron suppresses thermal line broadening, making the Fe K line width a sensitive probe of bulk gas motion. For line broadening studies, only one mock *Astro-E2* image of each cluster centered on the most bound position is used, giving a total of 1,836 observations. For this study, our final spectra are generated by requiring 400 counts in the line region (6.0-6.2 keV). The velocity broadenings of the spectra are returned as the parameter σ_v of the BAPEC fit.

Once again, we perform a theoretical check on these results. The EM-weighted velocity dispersion of the particles within the *Astro-E2* field of view is taken to be a predictor of the best-fit BAPEC σ_v parameter. The differences between these two measures of velocity broadening are shown in Figure 5. The dispersion for the entire data set of 1,836 broadenings is 55 km s^{-1}.

The data of Figure 5 show evidence of a systematic effect. The mean value of $\sigma_v(BAPEC) - \sigma_v(EM)$ is clearly offset from zero. For the complete sample, it is -26.6 km s^{-1} (median -25.4 km s^{-1}). This systematic is at least partly explained by the fitting process. The

[7] see http://heasarc.gsfc.nasa.gov/docs/software/ftools/ftools_menu.html

[8] see ftp://legacy.gsfc.nasa.gov/astroe2/nra_info/astroe2_td.pdf

spectral resolution (FWHM) of the XRS is about 6.5 eV, corresponding to a response contribution to the broadening of $\sigma_r = 1.5$ eV or ~ 75 km s^{-1} near the Fe Kα line. This implies that XSPEC should be unable to recognize physical broadenings significantly less than 75 km s^{-1} in our spectra. Clusters with EM-weighted broadenings significantly less than 75 km/s are therefore reported as zero broadening in the BAPEC fit.

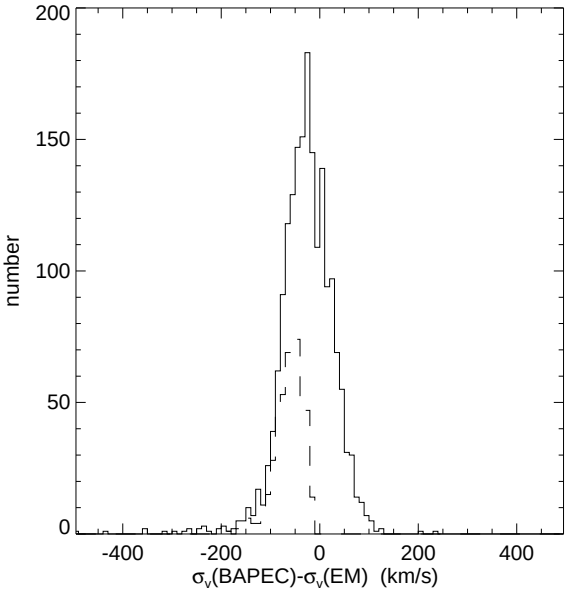

FIG. 5.— Histogram of the differences between the velocity broadening parameter returned by BAPEC and the EM-weighted velocity dispersion. The dashed line denotes the portion of the sample with BAPEC uncertainties $> 5\sigma_v$(BAPEC) (the "zero broadening" sample).

An investigation of this interpretation can be made using the BAPEC-reported uncertainty in the broadening value returned. If we divide the uncertainty in the broadening parameter by the value of the parameter, we expect to obtain a large number for spectra with broadenings that fall below the resolution of the XRS instrument. As a test, we construct this ratio and consider any spectrum with a broadening uncertainty greater than five times the broadening value to belong to the "zero-broadening sample". Implementing this definition yields a zero-broadening sample of 492 clusters which has a mean velocity broadening reported by BAPEC of 9.0×10^{-3} km s^{-1} (median 1.8×10^{-4} km s^{-1}) and a standard deviation of 0.025 km s^{-1}. These numbers are well below the resolution of the XRS instrument, confirming our intuition that a significant fraction of the overall cluster sample have physical broadenings unresolvable by XRS. The contribution of this zero-broadening sample to the histogram of Figure 5 is shown as a long-dashed line. Removing projections with zero reported broadening shifts the mean value of $\sigma_v(BAPEC) - \sigma_v(EM)$ to -13.4 km s^{-1} (median -10.4 km s^{-1}) and leaves the dispersion unchanged.

3. RESULTS

3.1. *Velocity Gradients*

Figure 6 shows the cumulative frequency distribution of velocity differences, normalized to the sound speed in the ICM, that result from the four-pointing tiling program. Because the ICM temperature is determined by the gravitational potential ϕ of a cluster, the sound speed in the ICM gas is approximately

$$c_s = \sqrt{\frac{5kT_{ICM}}{3\mu m_p}} \lesssim \sqrt{\phi} \qquad (1)$$

where μm_p is the average mass per ICM particle. Since the bulk velocity structure of the ICM is determined by mergers also driven by the gravitational potential of the dominant cluster, one expects infall velocities

$$v_{\rm inf} \approx \sqrt{2\phi}. \qquad (2)$$

All explicit dependence on ϕ, hence on the size of the cluster, vanishes when infall velocity is scaled by the sound speed.

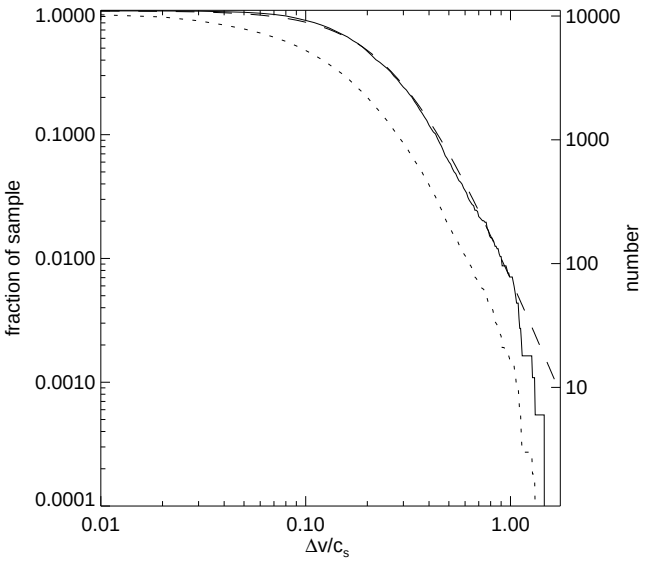

FIG. 6.— Cumulative likelihoods of the normalized velocity gradients $\Delta v/c_s$ are shown for the case of only maximum velocity differences (solid) and the case of all pointing pairs (dotted). A fit to the former is given by equation (3) (dashed).

For each simulation, we determine the sound speed from the best-fit spectral temperature of an isothermal fit to the $0.5 - 9.5$ keV emission of plasma within r_{500}, the radius within which the mean interior density is 500 times the critical value. This radius generally encloses several thousand of the gas particles making up the simulated cluster. The $0.5 - 9.5$ keV spectra are created by interpolating on a reference table of isothermal plasma emission spectra to find the contribution from each gas particle, and then summing these contributions to obtain the complete spectrum. The procedure is the same as that outlined in §2.2 for creating mock Fe Kα line spectra, except that the table of reference spectra for interpolation is generated using the MEKAL plasma emission code (Mewe, Kaastra & Liedahl 1995) and the spectral resolution is 150 eV per bin. The best-fit spectral temperature is determined by minimizing the chi-square of the residuals generated by differencing the complete $0.5 - 9.5$ keV spectrum of the simulation with isothermal plasma spectra created using MEKAL.

The solid line in Figure 6 shows the cumulative frequency distribution of the maximum velocity gradient among the six pairs of each four-pointing mosaic. The

fraction of cluster projections in the sample of 1,836 with a maximum normalized velocity difference larger than some value x is well fit by

$$f(\Delta v_{max}/c_s > x) \approx \left(1 + \left(\frac{x}{0.30}\right)^2\right)^{-2}. \quad (3)$$

The number of cluster projections in our sample with a maximum normalized velocity difference larger than half the sound speed for the cluster is 111, or approximately 6.0% of the sample. The total number of splittings out of the 11,016 measured to be larger than $0.5c_s$ is 200, or approximately 1.8%.

The likelihood of high Mach number splittings falls off dramatically, as $(\Delta v/c_s)^{-4}$. The lack of very high Mach collisions is expected from the arguments given in equations (1) and (2) above. One anticipates $v_{\rm inf} \lesssim$ a few $\times c_s$ because larger Mach numbers could not be generated by hierarchical clustering driven by gravity. Our mock spectral measurements are consistent with this expectation. Note that the quoted value of the sound speed always refers to the dominant member of a merging pair. With respect to c_s of the smaller member, high Mach number collisions are certainly possible. But the measured "broad-beam" temperature, and sound speed, of the merging system will always be driven by the larger member, and thus the data presented in Figure 6 are appropriate for comparison with observation.

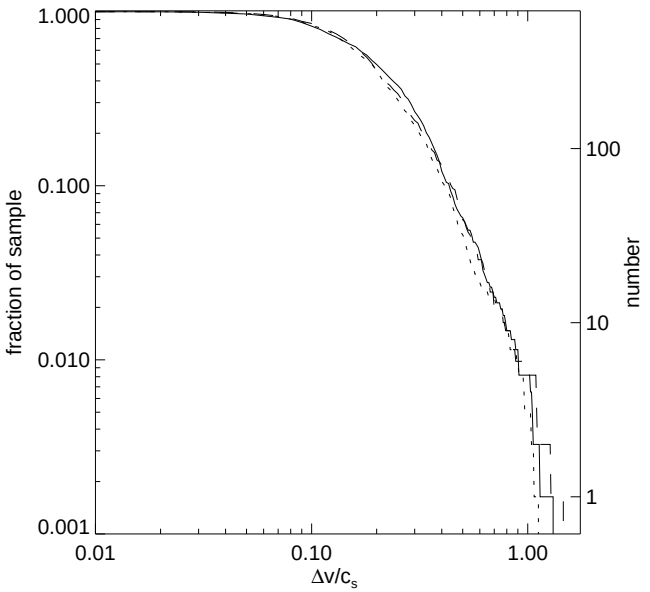

FIG. 7.— Cumulative likelihoods of the normalized velocity gradients $\Delta v/c_s$ are shown for the case of maximum velocity in three subsamples grouped according to simulation output redshift. The short-dashed line is the subsample of clusters at $z \geq 0.365$, the long-dashed line is clusters at $0.365 > z > 0.102$, and the solid line is clusters at $z \leq 0.102$.

It is important to recognize that even though all clusters have been moved to a fiducial redshift of $z = 0.1$ to construct mock observations, we have used clusters recovered from a simulated sample at several different output redshifts ranging from $z = 0.540$ to $z = 0$. It is therefore natural to ask if the frequency of large velocity gradients depends on the epoch of observation of the cluster sample. To address this question, we have constructed the cumulative frequency distribution of the maximum observed normalized velocity gradient for three subsamples grouped by simulation output redshift. The results are shown in Figure 7. The Kolmogorov-Smirnov (K-S) test (see, *e.g.*, Press et al. 1992) returns a 48.9% likelihood that the high redshift and middle redshift subsamples follow the same distribution, a 44.5% likelihood that the low and middle redshift subsamples follow the same distribution, and an 8.1% likelihood that the high and low redshift subsamples follow the same distribution.

Another question to consider is whether the size of the *Astro-E2* FOV relative to the cluster's size plays a role in the frequency of large velocity splittings observed. We address this by constructing the cumulative frequency distribution of the maximum observed normalized velocity gradient for two subsamples grouped by the physical size of the cluster (recall that all clusters are placed at the same fiducial redshift for observation, so that physical size corresponds directly to angular size). Clusters with an r_{200} larger than 1.46 Mpc (the median value for our sample) make up the large cluster subsample, while clusters with $r_{200} < 1.46$ Mpc form the small cluster subsample. The resulting distributions are shown in Figure 8. The K-S test gives a 58.6% likelihood that both subsamples follow the same distribution.

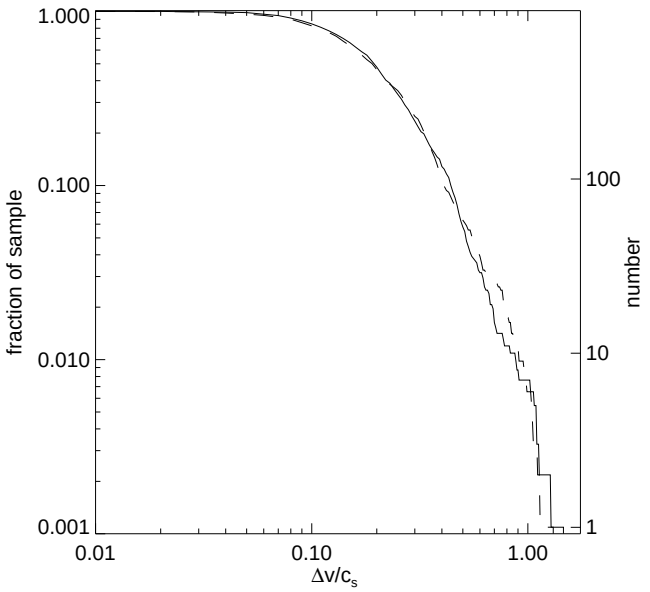

FIG. 8.— Cumulative likelihoods of the normalized velocity gradients $\Delta v/c_s$ are shown for the case of maximum velocity in two equal subsamples grouped according to cluster size. The dashed line is the subsample of clusters with $r_{200} < 1.46$ Mpc, the solid line is clusters with $r_{200} > 1.46$ Mpc.

For purposes of illustration, we highlight the cluster which exhibits the maximum velocity gradient: cluster number 2 at output redshift 0.222 in y-axis projection. This projection yields a maximum normalized velocity gradient of 1.47 c_s. Data relevant to that cluster are compiled in Figures 9-13. Figure 9 shows Poisson realizations of the four-point mosaic spectra created using the procedure outlined in §2.2 and grouped using the procedure explained in §2.4. These spectra show that the top two quadrants of our observing pattern are blueshifted relative to the bottom two. This accurately represents the underlying motion of the cluster, as can be seen from Figure 10 which shows the perfect flux spectra generated from the simula-

tion overlaid with the BAPEC fits to the spectra of Figure 9.

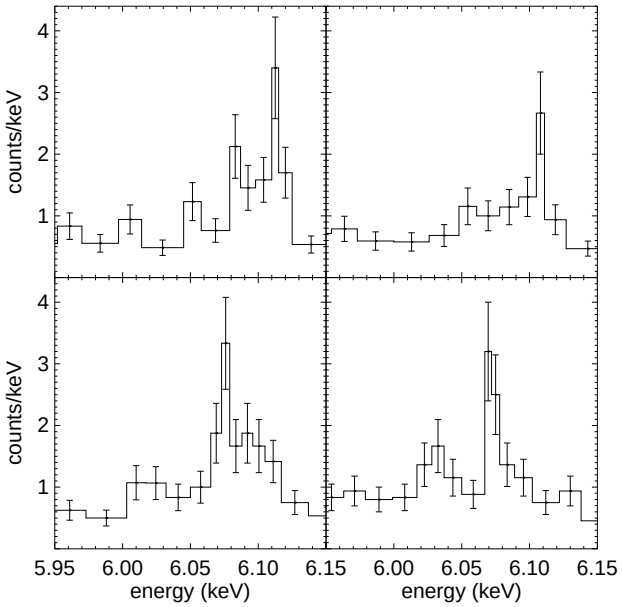

FIG. 9.— The integrated and grouped Poisson-noised spectra used in the velocity gradient study for cluster 2 at $z = 0.222$, viewed along the y-axis. The spectra are generated with the cluster at a fiducial redshift of 0.1. Each panel displays the spectrum of the corresponding four-point mosaic tile pattern shown in Figure 12.

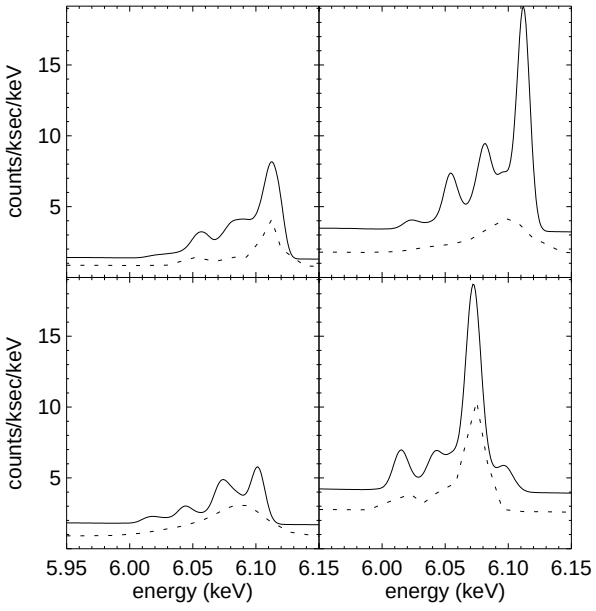

FIG. 10.— The flux spectra generated using the APEC thermal plasma code (solid) for cluster 2 at $z = 0.222$ are shown along with the BAPEC fits to the Poisson spectra of Figure 9 (dashed). The spectra are generated with the cluster at a fiducial redshift of 0.1.

The advantage of using simulations is that we can examine the underlying cause of this observed velocity structure. Figure 11 shows the density-weighted, LOS velocity map of the gas in cluster 2 in a region $2r_{200}$ on a side. A strong vertical gradient in projected velocity is apparent. The lower row of images in Figures 12 and 13 shows the z-axis (orthogonal view) surface brightness and temperature maps of cluster 2 at output redshifts $z = 0.290$, 0.222 and 0.160. With this additional information, we can see that cluster 2 is extremely active. In this case it appears that the redshifted quadrants (the lower half of the mosaic) represent the primary cluster itself, which has a peculiar velocity away from the observer. The blueshifted quadrants appear to contain a merging subcluster which is moving through the core in the negative y-direction. This subcluster can be traced in the z-axis projections starting in the upper left corner and moving toward the lower right over the course of the outputs presented in Figure 12.

see file figure11.jpg

FIG. 11.— The line-of-sight velocity map for cluster 2, $z = 0.222$ projected along the y-axis is shown along with the mock *Astro-E2* fields of view. The scale key is in km s^{-1}, with positive velocities away from the observer. The map size is $2r_{200}$ on a side.

3.2. *Line Broadening*

To evaluate the significance of the observed line broadenings, we normalize σ_v recovered from BAPEC by the expected thermal velocity dispersion ($\sigma_{th} = \sqrt{kT/m_{\rm Fe}}$). The resulting velocity dispersion distribution is presented in Figure 14. The distribution ignores $\sim 27\%$ of the fits that return zero for the velocity broadening parameter (see §2.5). The distribution of non-zero values is fit reasonably well by

$$f(\sigma_v/\sigma_{th} > x) \approx 0.73 \left(1 + \left(\frac{x}{1.5}\right)^3\right)^{-4/3} . \qquad (4)$$

Out of the whole sample, 902 cluster projections, or 49%, yield a BAPEC velocity dispersion larger than the thermal broadening of the cluster. As in the gradient case, the probability drops as $(\sigma_v/\sigma_{th})^{-4}$.

As we did for the velocity gradient study, we can also consider the impact of the epoch of observation and of the relative size of the *Astro-E2* FOV on the results of Figure 14. To determine if our results are dependent on the epoch of observation, we again construct three subsamples grouped by simulation output redshift and generate the cumulative frequency of normalized velocity broadenings for each subsample. The results are shown in Figure 15. The K-S test returns an 89.5% likelihood that the high redshift and middle redshift subsamples follow the same distribution, a 29.3% likelihood that the middle and low redshift

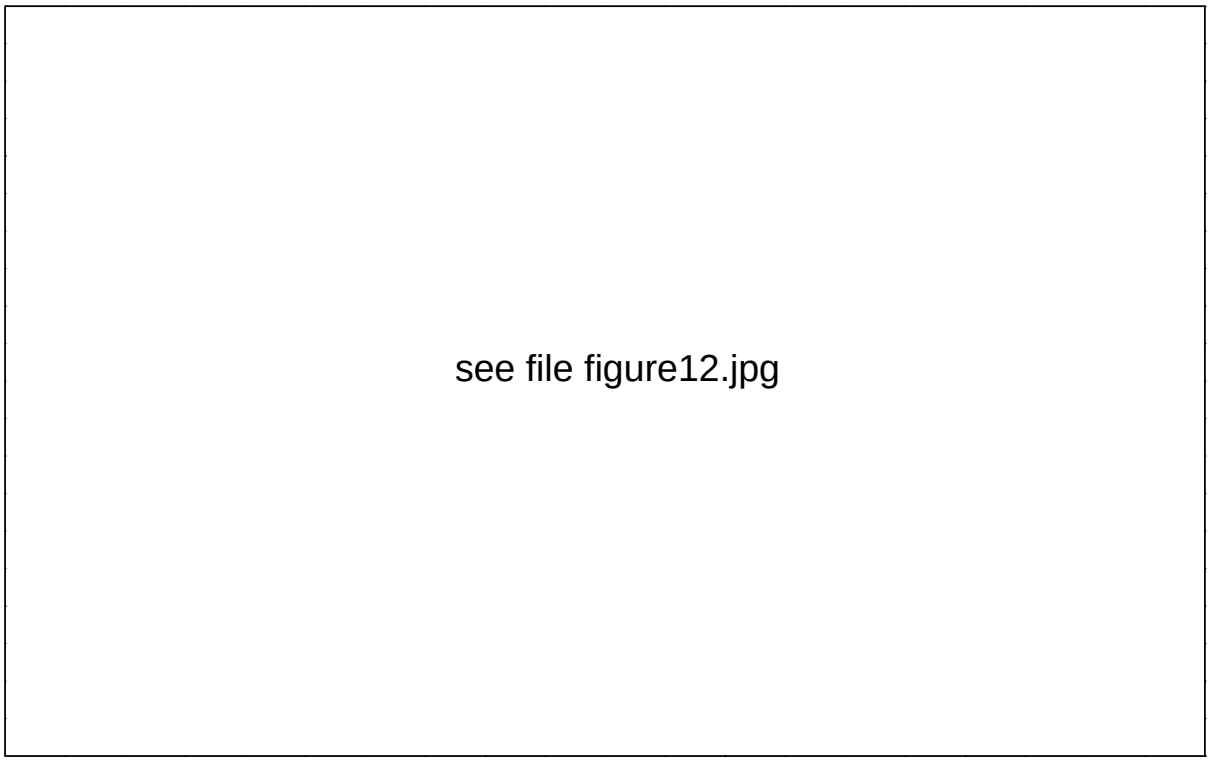

FIG. 12.— Maps show the log of the unabsorbed soft (0.5-2 keV) X-ray surface brightness (arbitrary units) for cluster 2 at output redshifts 0.290 (left), 0.222 (middle) and 0.160 (right), projected along the y (top) and z (bottom) axes of the simulation volume. The width of the image box is scaled to $2\,r_{200}$ at each epoch. The mock *Astro-E2* fields of view are overlaid on the frame that displays a velocity gradient $\Delta v = 1.47 c_s$. Note that although this map places the observer along the positive y-axis, the spectra were generated with positive y-axis velocity yielding redshift and negative y-axis velocity giving blueshift.

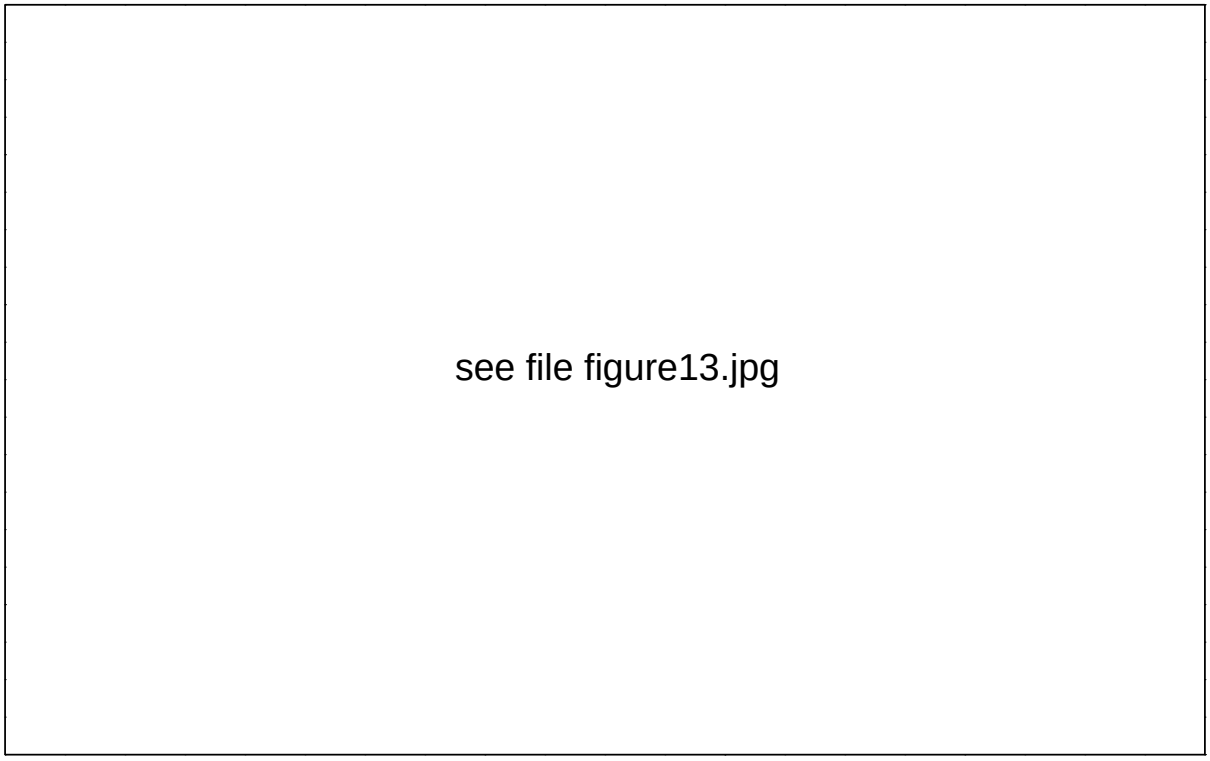

FIG. 13.— Temperature maps (keV) for cluster 2 at output redshifts 0.290 (left), 0.222 (middle), and 0.160 (right) along the x (top) and y (bottom) axes.

subsamples follow the same distribution, and a 26.2% likelihood that the high and low redshift subsamples follow the same distribution.

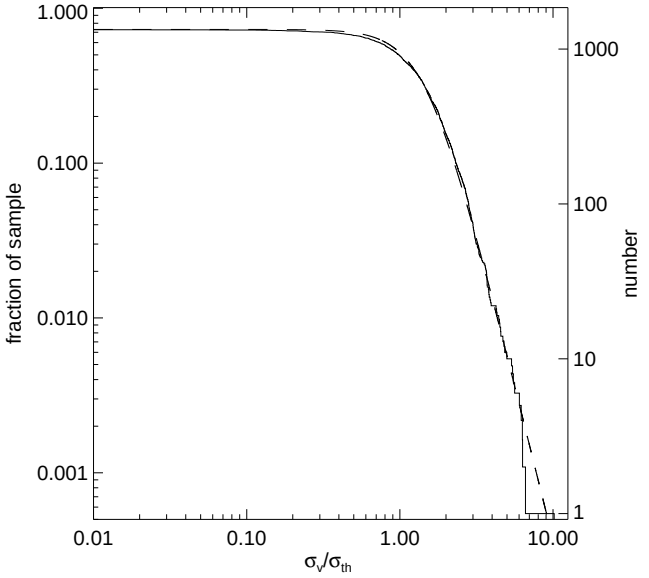

FIG. 14.— Fraction of sample with normalized velocity broadening greater than the x-axis value. The dashed line represents the fit given in equation (4).

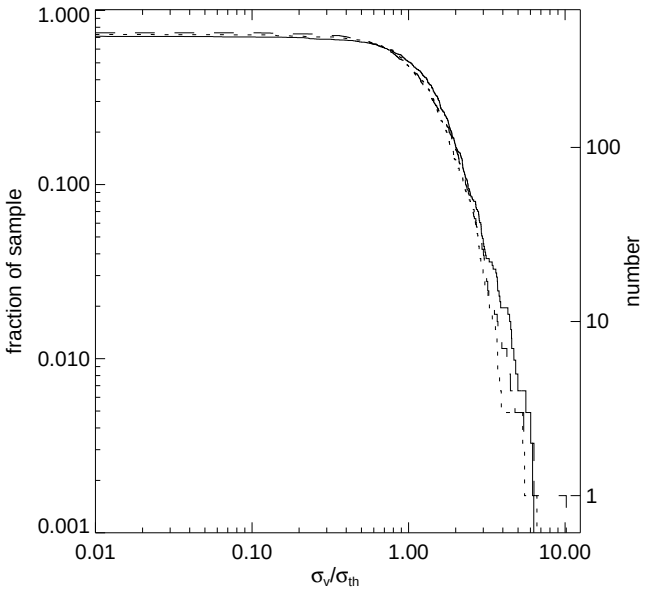

FIG. 15.— Cumulative likelihoods of the normalized velocity broadening for three subsamples grouped according to simulation output redshift. The short-dashed line is the subsample of clusters at $z \geq 0.365$, the long-dashed line is clusters at $0.365 > z > 0.102$, and the solid line is clusters at $z \leq 0.102$.

To evaluate the significance of the size of the *Astro-E2* FOV on the observed clusters, we create two subsamples grouped by the physical size of the cluster. The resulting cumulative frequency distributions are shown in Figure 16. For these distributions a K-S test is inappropriate because the result is dominated by the different sizes of the "zero-broadening" component of each subsample. Recall from §2.5 that clusters with velocity broadenings less than about 50 km s^{-1} are expected to be unresolved by the XRS instrument. Clusters with smaller physical sizes are expected to have smaller physical broadenings. This fact implies that the small cluster subsample should exhibit a larger fraction of broadenings below the resolution of the XRS instrument than the large cluster subsample does. This effect is seen in the low-broadening limiting values of the distributions of Figure 16. This difference dominates the K-S test, resulting in a likelihood of 1.5×10^{-7} that the large cluster and small cluster subsamples follow the same distribution. If we perform the K-S test without including differences in the region $\sigma_v/\sigma_{th} < 2$ we find a 98% likelihood that the distributions are the same, implying that the apparent divergence at large broadenings is statistically insignificant.

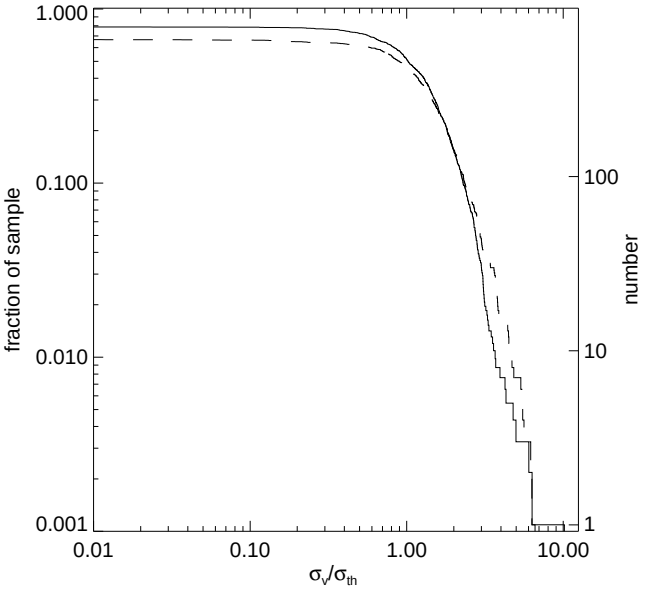

FIG. 16.— Cumulative likelihoods of the normalized velocity broadening for two equal subsamples grouped according to cluster size. The dashed line is the subsample of clusters with $r_{200} < 1.46$ Mpc, the solid line is clusters with $r_{200} > 1.46$ Mpc.

Once again, we select one cluster projection to highlight as a case study. We select the cluster which exhibited the most significant line broadening: cluster 47 at output redshift 0.222 viewed along the x-axis. The data relevant to this cluster is compiled in Figures 17-20. Again it is apparent that the cluster is undergoing a strong merger at this epoch. In this case, however, the merging cluster is almost directly behind cluster 47 (rather than slightly off-center as in the case of cluster 2 output redshift 0.222 shown above). This on-axis configuration means that all *Astro-E2* spectra in the four-pointing mosaic contain emission from the merging cluster, resulting in nearly identical (two-component) spectra. For this reason, each image in the multiple-pointing study gives approximately the same redshift when fit with a single-component plasma emission model, and differencing multiple images yields small velocity gradients. In fact, while this projection gives a velocity dispersion more than ten times the thermal velocity broadening, its maximum velocity gradient in the four-pointing mosaic is $0.63c_s$. This illustrates the complementarity of line broadening and multiple-imaging studies for detecting dynamically active clusters.

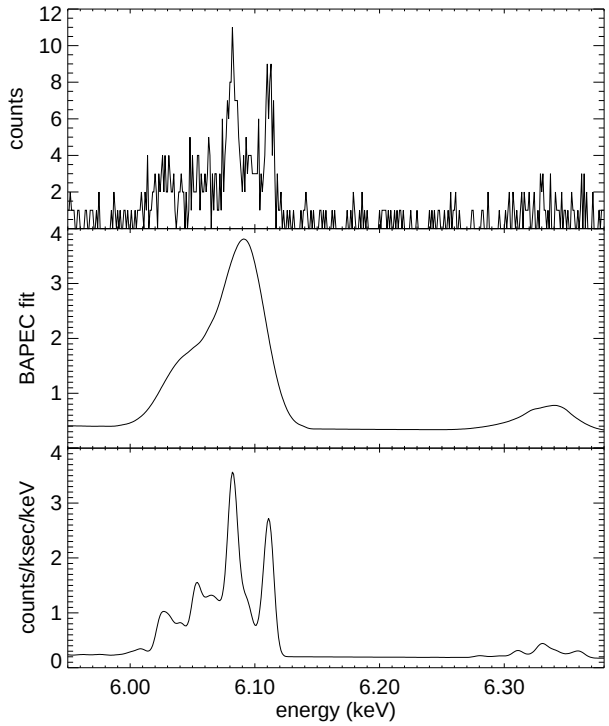

FIG. 17.— From top to bottom: the integrated spectrum, BAPEC fit, and actual flux spectrum for cluster 47, output at redshift 0.222, taken along the x-axis. The spectra are generated with the cluster at a fiducial redshift of 0.1.

see file figure18.jpg

FIG. 18.— Radial velocity map for cluster 47, output redshift 0.222 projected along the x-axis in the same format as Figure 11.

4. CONCLUSIONS

We use a large statistical sample of mock *Astro-E2* observations to investigate the expected frequency of detection of bulk motion of the ICM using the Fe XXV Kα line. We analyze differences in mean velocities among adjoining pointings as well as velocity broadenings in a single central pointing of clusters developed in a ΛCDM model and scaled to an observed redshift $z=0.1$. The mean velocities and broadenings are recovered from BAPEC fits to mock *Astro-E2* spectra assuming 200 counts and 400 counts in the line region, respectively.

From the central pointings, we find that roughly one-half of randomly selected clusters display velocity broadening in the Fe Kα line at least as large as the thermal width, and more than 15% will be broadened at a level greater than $2\sigma_{th}$. In the four-point mosaic case, 6% of clusters show a maximum velocity difference that is transonic ($\Delta v/c_s \geq 0.5$) while only 0.7% will be supersonic ($\Delta v/c_s \geq 1$).

These fractions were obtained without any attempt to select for interesting clusters or to optimally align observations on the basis of morphology. Further, our sample is biased toward cooler (smaller) clusters. We have attempted to remove the effects of this bias by normalization, but the physical cut represented by the ~ 75 km s^{-1} resolution of the XRS instrument cannot be normalized away. We can only assume that an observational survey, conducted to optimize results by selecting hot clusters with bimodal galaxy velocity distributions would obtain a sample with an even larger fraction of dynamically interesting clusters.

In extreme cases, however, morphological clues from X-ray observations can be misleading. We have illustrated one example in which the viewing angle is nearly aligned with the infall direction of a merging satellite. Such cases possess relatively simple X-ray morphologies but show large velocity effects in the Fe Kα line.

This calibration exercise bears out the expectation that *Astro-E2* will be an important instrument for detecting bulk motion of ICM gas. With reasonable counting statistics, the true emission-weighted velocity within the *Astro-E2* FOV can be obtained to within ~ 50 km s^{-1}, assuming the pre-launch gain and response estimates are accurate and that background is negligible.

We are very grateful to K. Arnaud for providing valuable input on spectral analysis tools. We also thank E. Figueroa for providing helpful information about *Astro-E2* gain. AP thanks J. Bialek for assistance with the manipulation of the VCE dataset and maps.

This work was supported by NASA through *Chandra* Theory grants TM3-4009X and TM4-5008X and by the NSF through ITR grant ACI-0121671. RAD also acknowledges support from NASA Grants NAG 5-3247 and *Chandra* GO3-4162X. AEE acknowledges support from a JSPS Invitation Fellowship to Tokyo University and thanks Y. Suto for hospitality.

FITS format spectra and maps similar to those presented in this paper are available on the VCE website for selected cluster projections used in this study, including all those which exhibited splittings greater than $0.75c_s$ or broadenings larger than $2.5\sigma_{th}$.

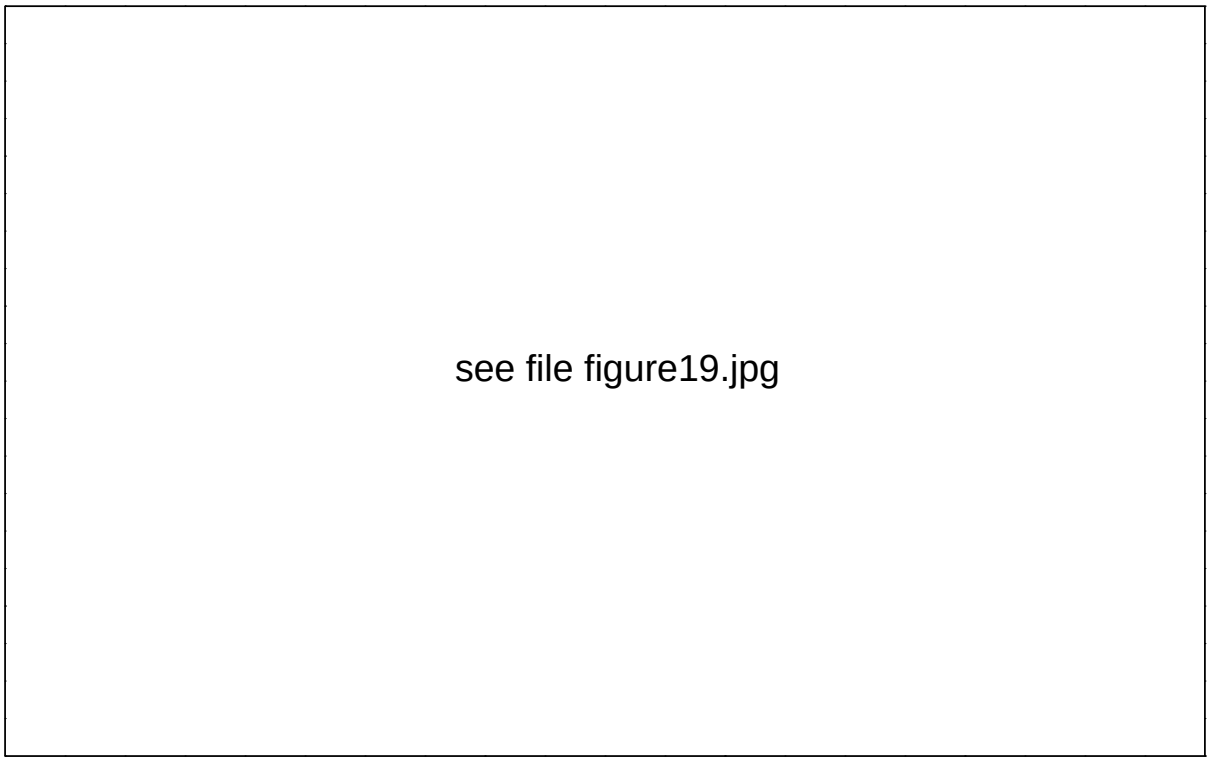

FIG. 19.— Maps show the log of the unabsorbed soft (0.5-2 keV) X-ray surface brightness (arbitrary units) for cluster 47 at output redshifts 0.290 (left), 0.222 (middle) and 0.160 (right), projected along the x (top) and y (bottom) axes of the simulation volume. The width of the image box is scaled to $2r_{200}$ at each epoch. The mock *Astro-E2* fields of view are overlaid on the frame that displays the largest velocity broadening of the sample. Note that although this map places the observer along the positive x-axis, the spectra were generated with positive x-axis velocity yielding redshift and negative x-axis velocity giving blueshift.

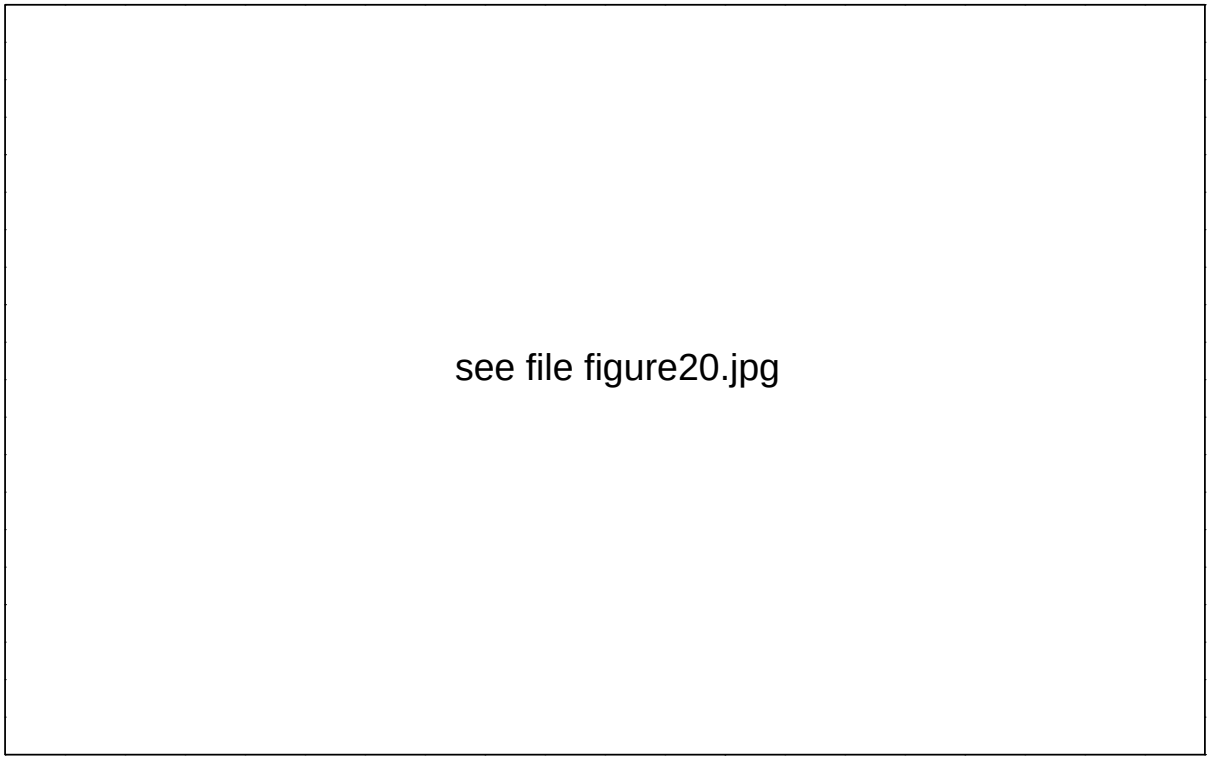

FIG. 20.— Temperature maps (keV) for cluster 47 at output redshifts 0.290 (left), 0.222 (middle) and 0.160 (right) along the x (top) and y (bottom) axes.

APPENDIX

COMPUTING OPTICAL DEPTH

The optical depth for line emission obeys (Spitzer 1978):

$$\int \tau(\nu)d\nu = f_{jk}N_j\frac{\pi e^2}{m_e c}\left(1-\frac{b_k}{b_j}e^{-h\nu_{jk}/kT}\right) \tag{A1}$$

where j and k label atomic states, ν_{jk} is the central frequency of the line radiation emitted in a transition from $k \rightarrow j$, f_{jk} is the upward oscillator stregth for the transition, and N_j is the column density of atoms/ions in state j. The quantities b_k and b_j measure the particle densities n_k and n_j relative to the values they would have in thermodynamic equilibrium (see Spitzer (1978) for details). At ICM densities, we expect $b_k = 0$ for the Fe Kα line (Dere et al. 1997; Young et al. 2003). The oscillator strength for the Kα line of Fe XXV is 0.798 (Verner et al. 1996). In cgs units, then:

$$\int \tau(\nu)d\nu \approx 0.0212N_j \tag{A2}$$

where N_j is the column density (in cm^{-2}) of Fe XXV in the ground state.

We next simplify things by defining an average optical depth for the line:

$$2\sqrt{2}\,\bar{\tau}\nu_{jk}\frac{\sigma_{jk}}{c} \equiv \int \tau(\nu)d\nu \tag{A3}$$

where we define a Gaussian sigma parameterizing the width of the Fe Kα line. In the terminology of this paper, we use the definition:

$$\sigma_{jk} \equiv \sqrt{\sigma_{th}^2+\sigma_v^2} \tag{A4}$$

(note that, in keeping with the rest of this work, we have chosen a σ in velocity units so that the combination σ/c is unitless). We have computed σ_{jk} for each cluster as a part of our line broadening study (see §3.2). We can now write (again, in cgs units):

$$\bar{\tau} \approx \frac{4.6\times10^{-21}cN_j}{\sqrt{\sigma_{th}^2+\sigma_v^2}}. \tag{A5}$$

The final quantity remaining to compute is N_j.

Assuming an iron abundance of 0.4 solar, we can write:

$$N_{Fe} \approx 2\times10^{-5}N_H. \tag{A6}$$

Not all the iron will be in the FeXXV ionization state, however. At maximum, 78% of the Fe will be Helium-like. This fraction has a non-negligible temperature dependence over the range of temperatures expected in the ICM. The peak occurs at a temperature of 3 keV. For temperatures below 1 keV or above 8 keV the fraction has fallen below 33%. For this reason, we use our knowledge of the underlying simulation to approximate the optical depth for resonant scattering in our sample of clusters. We define a function $f(T)$ using a linear interpolation on Table 4 of Arnaud & Raymond (1992). We then assign the ith gas parcel within the FOV a column density for resonant scattering given by:

$$N^i_{FeXXV} = 2\times10^{-5}f(T_i)N^i_H. \tag{A7}$$

We can then sum up the column densities in the FOV to find the average optical depth in the FOV:

$$\bar{\tau}_{FOV} = 9.2\times10^{-26}\sum_{i\in FOV}\frac{cf(T_i)N^i_H}{\sqrt{\sigma_{th}^2+\sigma_v^2}}. \tag{A8}$$

REFERENCES

Anders, E. & Grevesse, N. 1989, Geochim. Cosmochim. Acta, 53, 197
Arnaud, K.A. 1996, Astronomical Data Analysis Software and Systems V, eds. Jacoby, G. and Barnes, J., ASP Conf. Series volume 101 [http://heasarc.gsfc.nasa.gov/docs/xanadu/xspec/index.html]
Arnaud, M & Raymond, J. 1992, ApJ, 398, 394
Bennet, C.L., et al. 2003, ApJS, 148, 1
Bialek, J.J., Evrard, A.E. & Mohr, J.J. 2001, ApJ, 555, 597
Bialek, J.J., Evrard, A.E. & Mohr, J.J. 2002, ApJ, 587, L9
Bialek, J.J., Evrard, A.E. & Mohr, J.J. 2005, in preparation
Buote, D.A. & Tsai, J.C. 1996, ApJ, 458, 27
Churazov, E., Forman, W., Jones, C., Sunyaev, R. & Böhringer, H. 2004, MNRAS, 347, 29
De Grandi, S., Ettori, S., Longhetti & M. Molendi, S. 2004, A&A, 419, 7
Dere, et al. 1997, AASS, 125, 149
Dupke, R.A. & Arnaud, K.A. 2001, ApJ, 548, 141
Dupke, R.A. & Bregman, J.N. 2001a, ApJ, 547, 705
Dupke, R.A. & Bregman, J.N. 2001b, ApJ, 562, 266
Edge, A.C., Stewart, G.C. & Fabian, A.C. 1992, MNRAS, 258, 177
Evrard, A.E. 1988, MNRAS, 235, 911
Frenk, C.S., et al. 1999, ApJ, 525, 554
Fujita, Y., Matsumoto, T., Wada, K. & Furusho, T. 2005, ApJ, 619, L139
Furusho, T., Mitsuda, K., Yamasaki, N., Fujimoto, R., & Ohashi, T. 2004, astro-ph/0401490
Gastaldello, F. & Molendi, S. 2004, ApJ, 600, 670
Gil'fanov, M.R., Sunyaev, R.A. & Churazov, E.M. 1987, Pis'ma Astron. Zh. 13, 7
Inogamov, N.A. & Sunyaev, R.A. 2003, Astron. Lett., 29, 791
Jones, C. & Forman, W. 1984, ApJ, 276, 38
Mewe, R., Kaastra, J.S. & Liedahl, D.A. 1995, Legacy, 6, 16
Mohr, J.J., Fabricant, D.G. & Geller, M.J. 1993, ApJ, 413, 492
Molendi, S., Matt, G., Antonelli, L.A., Fiore, F., Fusco-Femiano, R., Kaastra, J., Maccarone, C. & Perola, C. 1998, ApJ 499, 608

Press, W.H., Teukolsky, S.A., Vetterling, W.T. & Flannery, B.P. 1992, *Numerical Recipies in Fortran, 2nd ed.*, Cambridge University Press
Smith, R.K., Brickhouse, N.S., Liedahl, D.A. & Raymond, J.C. 2001, ApJ 556, L91 [http://cxc.harvard.edu/atomdb//index.html]
Spitzer, L. 1978, *Physical Processes in the Interstellar Medium*, (Wiley, NY)
Sunyaev, R.A., Norman, M.L. & Bryan, G.L. 2003, Astron. Lett., 29, 783
Thomas, P.A. & Couchman, H.M.P 1992, MNRAS, 257, 11
Ulmer, M.P., Cruddace, R.G., Fritz, G.G., Snyder, W.A. & Fenimore, E.E. 1987, ApJ, 319, 118
Verner, D.A., Verner, E.M. & Ferland, G.J. 1996, Atomic Data and Nuclear Tables, 64, 1
White, R.E. III, Day, C.S.R., Hatsukade, I. & Hughes, J.P. 1994, ApJ, 433, 583
Young, et al. 2003, ApJSS, 144, 135

This figure "figure1.jpg" is available in "jpg" format from:

http://arXiv.org/ps/astro-ph/0503281v2


This figure "figure11.jpg" is available in "jpg" format from:
http://arXiv.org/ps/astro-ph/0503281v2


This figure "figure12.jpg" is available in "jpg" format from:
http://arXiv.org/ps/astro-ph/0503281v2


This figure "figure13.jpg" is available in "jpg" format from:
http://arXiv.org/ps/astro-ph/0503281v2


This figure "figure18.jpg" is available in "jpg" format from:
http://arXiv.org/ps/astro-ph/0503281v2


This figure "figure19.jpg" is available in "jpg" format from:
http://arXiv.org/ps/astro-ph/0503281v2


This figure "figure20.jpg" is available in "jpg" format from:
http://arXiv.org/ps/astro-ph/0503281v2